

# LATTICE AND CONTINUUM DAMAGE MODELING FOR FRACTURE OF CONCRETE

**Gilles Pijaudier-Cabot\***, **Julien Khoury\***, and **Gianluca Cusatis**<sup>†</sup>

\* Université de Pau et des Pays de l'Adour, CNRS, Laboratoire des Fluides Complexes et leurs Réservoirs  
Anglet 64600, France

e-mails: gilles.pijaudier-cabot@univ-pau.fr and julien.khoury@univ-pau.fr

<sup>†</sup>Northwestern University, Department of Civil and Environmental Engineering  
Evanston IL, 60208, USA

e-mail: g-cusatis@northwestern.edu

**Key words:** Lattice Discrete Particle Model, Continuum-based models, Coarse graining, Nonlocal damage

**Abstract.** Lattice modelling of quasi-brittle materials such as concrete is a discrete, meso-scale, description of the material in which constitutive relations are prescribed at a lower scale compared to the scale at which continuum-based constitutive relations are written usually. The mesostructure of the material is represented explicitly. Over the years, lattice models have become more and more efficient. Complex nonlinear responses at the macro-scale are obtained today, while keeping the constitutive model at the meso-scale simple compared to macro-scale ones. Prediction capabilities and accuracy of the description of the mechanical response at the global level are, in many cases, better than those obtained with continuum-based models, although at the price of an intensive computational effort. In this work, we intend to draw a parallel between the Lattice Discrete Particle Model (LDPM) and a macro-scale damage model. For this, we implement first a coarse graining approach based on averaging the equations of conservation to convert lattice results into coarse-grained, continuum-based, stress versus strain responses. Because stresses and strains are coarse-grained independently, their relationship yields a database of macroscopic continuum responses. These data are then used to calibrate a non-local damage model.

## 1 INTRODUCTION

The mechanical response of quasi-brittle materials such as concrete or rocks exhibit several characteristics depending on the type of loading. In most cases, when the state of stress does not involve too much triaxial compression, failure occurs due to crack propagation. Cracking observed in tension dominated responses is progressive. For instance, acoustic emission analyses of the failure of single edge notched bending beams (see e.g. [1, 2]) show that prior to macro-crack propagation, micro-cracking develops in

a large zone ahead of the tip of the macro-crack, the Fracture Process Zone (FPZ). The size of the FPZ is related to the size of the heterogeneities in the material e.g., it is a few times the maximum aggregate size.

The description of this progressive cracking process cannot be performed within Linear Elastic Fracture Mechanics (LEFM) which relates to a brittle response. There are two possibilities: one is to enhance LEFM with some type of cohesive law, thereby collapsing the FPZ onto a line where cohesive forces oppose to crack opening [3]. The second one is Contin-

uum Damage Mechanics (CDM). It provides a broad framework covering distributed cracking, macro-crack initiation, and then crack propagation within a single setting. Its application to quasi-brittle materials dates to the 1980's [4].

In the simplest version of damage models, micro-cracking is described by a single scalar variable that degrades the Young's modulus of the material. Accordingly, the effect of micro-cracking is isotropic. Introducing anisotropic damage adds complexity in the constitutive equations. In most cases, this is done by considering that damage is a second order tensor (see e.g., [5]), but there exists also some general framework that allow for more complex descriptions of damage in a material [6]). Further, permanent (plastic) strains do not exist in a scalar damage model, although they are measured experimentally. This is the reason why continuum damage has been coupled to plasticity, in most cases damage being still defined as a scalar variable (see e.g., [7]).

Without doubts, achieving a better description of the material response in a continuous setting yields more and more complex constitutive models, involving a growing number of material parameters and calling for more and more experiments for calibration purposes. This consideration motivated researchers to streamline the number of material parameters as much as possible, still relying on continuum damage mechanics to describe the tensile response. One may distinguish again two possibilities: in the first one, the material response is defined at the level of facets, within a continuum setting. This is exactly what is performed in the microplane model (see the M7 version in [8]). In a recent paper, Bažant, and co-workers showed the superior capability of such a model, compared to other approaches for fracture, at describing a wide variety of experiments on concrete [9]. The second possibility is to depart from a continuum description of the material and to use a lattice approach. The microstructure of the material is introduced in the model explicitly, and the overall mechanical response is the result of the interactions between discrete

particles depicted mechanically with nonlinear bonds. Inherently, because the bonds have specific orientations due to the discrete description of the microstructure, the material behavior is defined on facets, same as in the microplane model.

In a sense, lattice models could be viewed as the result of constraining the facets orientations in the microplane model to the microstructure of the material. Instead of defining all possible facets and integrating the response over a sphere, what is typically done in microplane models, in these lattice models there is a finite number of possible facets resulting from the discrete description of the material. Following the pioneering works of Cundall, Bažant and co-workers [10, 11, 12], the lattice approach has been widely developed (see the review in [13]).

Lattice calculations can accurately describe the mechanical response of geomaterials ([14]). However, solving for equilibrium, requires the resolution of a high number of unknowns, which needs extensive computational resources. Reducing the magnitude of the problem is critical for practical implementations [15]. Combining LDPM with classical finite elements is one method for reducing the size of the problem to be solved. LDPM is put in places where a nonlinear response is needed and classical finite elements are used elsewhere, following an elastic response [16]. Another way is to upscale the lattice response to a macro-scale continuum one that can serve as a reference either for calibration of a macro-scale continuum constitutive relation, or used in some data driven approach [17]. In this contribution, we investigate the potential of upscaling approaches.

## 2 LATTICE DISCRETE PARTICLE MODEL

Originally developed by Cusatis and colleagues [18], the Lattice Discrete Particle Model (LDPM) is a meso-scale model designed to simulate particle interactions in granular materials, including mortar [19], engineered cementitious composites [21], concrete and fiber reinforced concrete [20, 22]. In this model,

spherical particles representing the grain size distribution of the materials are arranged in the sample from the largest to the smallest size. A Delaunay tetrahedralization of the particle centers, along with nodes forming the external mesh, defines the lattice system. The domain is then tessellated, creating a network of polyhedral cells surrounding each spherical particle. The intersections of these cells are represented by triangular facets, where stresses and strains are expressed in vectorial form. Figure 1 provides an example of two adjacent polyhedral cells.

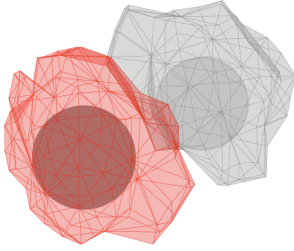


Figure 1: Polyhedral Cells surrounding the LDPM grains.

LDPM incorporates specific constitutive equations to describe tensile fracturing with strain softening, cohesive and frictional shearing, and compressive response with strain-hardening. Since this study focuses on concrete fracturing, the corresponding constitutive laws are recalled only.

If  $\mathbf{x}_i$  and  $\mathbf{x}_j$  denote the positions of nodes  $i$  and  $j$ , adjacent to the facet  $k$ , the facet strain vector is defined as:

$$\begin{aligned} \mathbf{e}_k &= [e_{N_k} \ e_{M_k} \ e_{L_k}]^t \\ &= \left[ \frac{\mathbf{n}_k^t \llbracket \mathbf{u}_k \rrbracket}{l_k} \ \frac{\mathbf{m}_k^t \llbracket \mathbf{u}_k \rrbracket}{l_k} \ \frac{\mathbf{l}_k^t \llbracket \mathbf{u}_k \rrbracket}{l_k} \right]^t \end{aligned} \quad (1)$$

where  $e_{N_k}$  is the normal strain component, and  $e_{M_k}$  and  $e_{L_k}$  are the tangential strain components,  $\llbracket \mathbf{u}_k \rrbracket = \mathbf{u}_j - \mathbf{u}_i$  is the displacement jump corresponding to facet  $k$ ,  $l_k = \|\mathbf{x}_j - \mathbf{x}_i\|$  is the distance between the two nodes,  $\mathbf{n}_k = (\mathbf{x}_j - \mathbf{x}_i)/l_k$  and  $\mathbf{m}_k$  and  $\mathbf{l}_k$  are two unit vectors mutually orthogonal in the facet plane projected orthogonally to the line connecting the adjacent nodes.

The stress vector on facet  $k$  is defined as  $\mathbf{t}_k = [t_{N_k} \ t_{M_k} \ t_{L_k}]^t$ , where  $t_{N_k}$  is the normal component, and  $t_{M_k}$  and  $t_{L_k}$  are the shear components. For the sake of readability, the subscript  $k$  that designates the facet is further dropped. The elastic behavior is formulated through linear relations between the normal and shear stress vector components, and the corresponding strain vector components as follows:

$$t_N = E_N e_N, \quad t_M = E_T e_M, \quad t_L = E_T e_L \quad (2)$$

where  $E_N = E_0$  and  $E_T = \alpha_0 E_0$ .  $E_0 \approx E/(1 - 2\nu)$  and  $\alpha_0 \approx (1 - 4\nu)/(1 + \nu)$  are the effective normal modulus and the shear-normal coupling parameter, respectively.  $E$  is the macroscopic Young's modulus and  $\nu$  is the macroscopic Poisson's ratio.

Concrete fracturing in mode I is always accompanied by shear at facets. This is a realistic feature since it is experimentally observed that most fracture paths are located at the interface between aggregates and cement paste. Therefore, the cohesive fracture behaviors in tension but also in tension-shear are important. This cohesive fracture occurs for  $e_N > 0$ . One can define an effective strain as  $e = (e_N^2 + \alpha_0(e_M^2 + e_L^2))^{\frac{1}{2}}$ , and an effective stress as  $t = (t_N^2 + (t_M^2 + t_L^2)/\alpha_0)^{\frac{1}{2}}$  and write the relationship between stresses and strains through  $t_N = t.(e_N/e)$ ,  $t_M = \alpha_0 t.(e_M/e)$  and  $t_L = \alpha_0 t.(e_L/e)$ . The effective stress  $t$  is defined incrementally as  $\dot{t} = E_N \dot{e}$  and its magnitude is limited by a strain-dependent boundary which is written as  $0 \leq t \leq \sigma_{bt}(e, \omega_{sn})$  where

$$\begin{aligned} \sigma_{bt}(e, \omega_{sn}) &= \sigma_0(\omega_{sn}) \\ &\exp \left[ -H_0(\omega_{sn}) \frac{\langle e_{\max} - e_0(\omega_{sn}) \rangle}{\sigma_0(\omega_{sn})} \right]. \end{aligned} \quad (3)$$

$\langle x \rangle = \max(x, 0)$ ,  $\omega_{sn}$  is a variable defining the level of interaction between shear and normal loadings. It is defined as  $\tan(\omega_{sn}) = (e_N)/(\sqrt{\alpha_0} e_T) = (t_N \sqrt{\alpha_0})/(t_T)$  where  $e_T$  is the total shear strain  $e_T = (e_M^2 + e_L^2)^{\frac{1}{2}}$ , and  $t_T$  is the total shear stress  $t_T = (t_M^2 + t_L^2)^{\frac{1}{2}}$ . The maximum effective strain is time dependent and is defined as  $e_{\max}(\tau) = (e_{N,\max}^2(\tau) +$

$\alpha_0 e_{T,\max}^2(\tau)^{\frac{1}{2}}$  where  $e_{N,\max}(\tau) = \max_{\tau' < \tau} [e_N(\tau')]$  and  $e_{T,\max}(\tau) = \max_{\tau' < \tau} [e_T(\tau')]$ . The strength limit of the effective stress that defines the transition between pure tension and pure shear is written as

$$\begin{aligned} \sigma_0(\omega_{sn}) &= \sigma_t \frac{-\sin(\omega_{sn})}{2\alpha_0 \cos^2(\omega_{sn})/r_{st}^2} \\ &+ \sigma_t \frac{(\sin^2(\omega_{sn}) + 4\alpha_0 \cos^2(\omega_{sn})/r_{st}^2)^{\frac{1}{2}}}{2\alpha_0 \cos^2(\omega_{sn})/r_{st}^2} \end{aligned} \quad (4)$$

where  $r_{st} = \sigma_s/\sigma_t$  is the ratio of the shear strength to the tensile strength,  $\sigma_s$  is the shear strength and  $\sigma_t$  is the tensile strength. The post-peak softening modulus is controlled by the effective softening modulus in Eq. (3)  $H_0(\omega_{sn}) = H_s/\alpha_0 + (H_t - H_s/\alpha_0)(2\omega_{sn}/\pi)^{n_t}$ , in which  $H_t = 2E_0/(l_t/l - 1)$ ,  $H_s = r_s E_0$  and  $n_t$  is the softening exponent. Typically, the values of  $n_t = 0.2$  and  $r_s = 0$  are assumed and are fixed.  $l_t$  is the tensile characteristic length defined as  $l_t = 2E_0 G_t/\sigma_t^2$  and  $G_t$  is the meso-scale fracture energy.

This LDPM model has been implemented in statics, as well as in dynamics, in the Cast3M finite element software.

### 3 COARSE GRAINING

The coarse-graining technique employed here is based upon conservation laws [23, 24]. First, the upscaled mass density is calculated from a weighted average of the local ones, defining a convolution product: convolution of  $x$  is  $(x)_\phi$ .

$$R(x) = (\rho(x))_\phi = \frac{\int_\Omega \rho(s)\phi(x, s)ds}{\int_\Omega \phi(x, s)ds} \quad (5)$$

where  $R$  is the macro-scale mass density,  $\rho$  is the mass density at mesoscale level,  $\phi$  is the convolution function described in Eq. (6), and  $\Omega$  is the domain of interest.

$$\phi(x, s) = \frac{1}{\frac{L_{CG}}{3}\sqrt{2\pi}} \exp\left\{\left(\frac{-(x-s)^2}{2\left(\frac{L_{CG}}{3}\right)^2}\right)\right\} \quad (6)$$

$L_{CG}$  is the coarse graining length. The mass balance at both scales is given by Eqs. (7, 8).

$$\frac{\partial \rho}{\partial t} + \nabla \cdot (\rho v) = 0 \quad (7)$$

$$\frac{\partial R}{\partial t} + \nabla \cdot (RV) = 0 \quad (8)$$

where  $\nabla \cdot (x)$  is the divergence of  $x$ ,  $v$  is the velocity field at meso-scale,  $V$  the velocity at macro-scale, and  $RV$  the impulsion. The partial time derivative of the coarse grained (macro-scale) mass density can be computed by taking the convolution of Eq. (7):

$$\frac{\partial R}{\partial t} = \frac{\partial \rho}{\partial t}_\phi = -\nabla \cdot (\rho v)_\phi \quad (9)$$

The macro-scale, coarse grained velocity in Eq. 10) is derived from Eqs. (8) and (9).

$$V = \frac{(\rho v)_\phi}{R} \quad (10)$$

It is a function of the meso-scale velocity field  $v$ , the local mass density  $\rho$  and the domain's coarse grained mass density  $R$ . Integrating velocities over time generates displacements, which are used to calculate strains, Eq. (11) shows the coarse-grained displacement  $U$  as a function of the meso-scale displacement field  $u$ , the local mass density  $\rho$ , and the domain's coarse grained mass density  $R$  for quasi-static problems.

$$U = \int_t V dt = \int_t \frac{(\rho u)_\phi}{R} dt \quad (11)$$

A similar procedure is applied for the balance of momentum. Meso and macro-scale conservation of the momentum read respectively:

$$\frac{\partial \rho v}{\partial t} + \nabla \cdot (\rho v \otimes v) = \nabla \cdot (\sigma) \quad (12)$$

$$\frac{\partial RV}{\partial t} + \nabla \cdot (RV \otimes V) = \nabla \cdot (S) \quad (13)$$

where  $\sigma$  represents the meso-scale stress field and  $S$  the macro-scale or coarse-grained stress. The convolution of Eq. (12) yields:

$$\begin{aligned} \frac{\partial RV}{\partial t} &= \frac{\partial(\rho v)_\phi}{\partial t} \\ &= (\nabla \cdot (\sigma) - \nabla \cdot (\rho v \otimes v))_\phi \end{aligned} \quad (14)$$

Introducing the fluctuating velocity  $v' = v - V$  and inserting it in Eq. (14) yields Eqs. (15) and (16), relating the coarse grained stress  $S$  to the meso-scale stress ( $\sigma$ ), mass density ( $\rho$ ), and fluctuation velocity ( $v'$ ):

$$\begin{aligned} \frac{\partial RV}{\partial t} + \nabla \cdot (RV \otimes V) &= \\ (\nabla \cdot (\sigma) - \nabla \cdot (\rho v' \otimes v'))_\phi & \end{aligned} \quad (15)$$

and then:

$$S = (\sigma - (\rho v' \otimes v'))_\phi \quad (16)$$

As this study primarily works with quasi-static computations, the effect of the fluctuating velocity is neglected. In other words, the coarse graining stress  $S$  may be defined using just meso-scale stress measurements  $S = (\sigma)_\phi$ . We conclude from Eqs. (11) and (16) that the macroscopic displacements and stresses are calculated separately by coarse graining the conservation equations.

Coarse-graining discrete results needs a preliminary step because LDPM results are defined by stress vectors at each facet and displacements at the center of each grain. In other words, there is no such a thing as a meso-scale stress tensor in the discrete model. A stress tensor at the center of each grain is estimated using the stress vectors of each polyhedral cell. For this purpose, Eq. (17) is solved after considering three unit uniaxial and three unit shear strain tensors.

$$\begin{aligned} & \text{Find } \sigma \text{ such that } \forall \varepsilon^* \\ & \sum_k [(\sigma \cdot n - t_k) \cdot (\varepsilon^* \cdot n)] = 0 \end{aligned} \quad (17)$$

To summarize, LDPM results are coarse grained and couples of stress and stress tensors are obtained independently at each loading step and everywhere. The process involves

a weighted average and therefore, there is a length that comes in the picture, the coarse graining length  $L_{CG}$ . It is important to underline that no constitutive relation is assumed at the macro-scale. The relationship between the coarse grained strains and stresses emanates from the meso-scale directly, accounting for the meso-structure of the material.

The coarse graining length is the sole parameter in the upscaling process that needs to be calibrated. This is performed by considering uniaxial loading on a cylindrical specimen in the elastic regime. Stresses and displacements are coarse-grained onto a regular grid of hexahedral elements of size ranges from 1/2.5 to less than 1/10 times the maximum aggregate size. Figure 2 shows the evolution of the average uniaxial stress for different values of the coarse graining length. We may observe that the average stress becomes quickly constant as the coarse graining length increases. On the same figure, the coefficient of variation of the coarse-grained stress distribution is plotted.

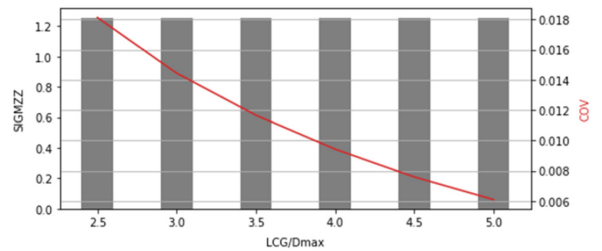


Figure 2: Influence of the coarse graining length on the stress and co-variance in the elastic regime.

The coarse graining length is obtained by setting the coefficient of variation less or equal to one percent. Compared to the maximum size of the aggregate in the meso-structure, we obtain  $L_{CG} = 4 \cdot D_{max}$  where  $D_{max}$  is the maximum aggregate size.

#### 4 CALIBRATION OF DAMAGE MODELS FROM A STRUCTURAL RESPONSE

A plain concrete single edge notched beam, measuring 700 mm in length, 200 mm in depth, and with a span-to-depth ratio of 2.5, is consid-

ered in this part. The notch thickness is 2 mm, and its length is 20% of the overall depth. The beam is loaded under three point bending. The geometry and load conditions correspond to the beams tested by Grégoire et al. [26]. Figure 3 shows the LDPM model. Five distinct samples have been generated, differing only in their geometrical particle distribution. Then, global responses have been averaged.

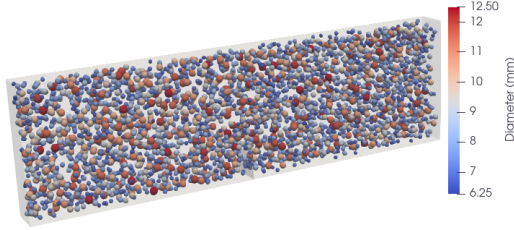


**Figure 3:** LDPM Particles in a Notched Beam Sample.

The main LDPM parameters are provided in the table below.

**Table 1:** LDPM Model Parameters.

|                                 |            |            |
|---------------------------------|------------|------------|
| Normal Modulus                  | $E_0$      | 43,195 MPa |
| Alpha                           | $\alpha$   | 0.25       |
| Tensile Strength                | $\sigma_t$ | 4.6 MPa    |
| Tensile Characteristic Strength | $l_t$      | 200 mm     |
| Shear Strength ratio            | $r_t$      | 2.5        |

Figure 4 shows the average load versus displacement response and figure 5 shows a typical failure, with a crack that starts to propagate upwards at the notch tip.

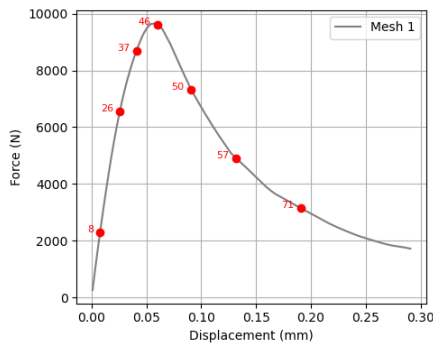


**Figure 4:** Averaged response of the beam and time steps at which coarse graining is performed.

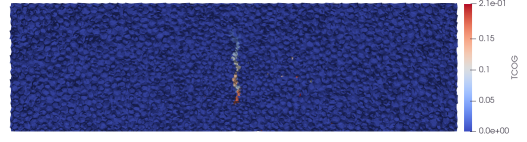


**Figure 5:** Crack Opening as obtained by LDPM.

A grid of hexahedral elements with sizes ranging from  $1/2.5D_{max}$  to less than  $1/10D_{max}$ , is considered for coarse-graining. Stresses and displacement are computed for the points shown in figure 6, and at the time steps shown in figure 4. To avoid edge effects, the window of points is placed above the notches such that it is far away from the edges.

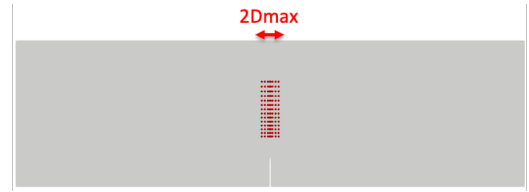


**Figure 6:** The coarse graining window. Red dots show coarse graining points.

Coarse-grained LDPM calculations are compared with continuum damage-based computations. The constitutive relation is defined in Eq. (18):

$$\sigma = (1 - D) \cdot C : \varepsilon \quad (18)$$

where  $\sigma$  is the second order stress tensor,  $\varepsilon$  is the second order strain tensor,  $C$  is the fourth order elastic stiffness tensor and  $D$  the damage scalar.  $D$  ranges from 0 for an undamaged material to 1 for a completely cracked material. The equivalent strain defined in Eq. (19) controls the progression of damage and the limit of the elastic behaviour is defined in Eq. (20) [27].

$$\tilde{\varepsilon} = \sqrt{\sum_{i=1}^3 \langle \varepsilon_i \rangle_+^2} \quad (19)$$

$$\mathbb{K}(x, t) = \max_{[0, t]} (\tilde{\varepsilon}(x, t), K_{tr0}) \quad (20)$$

where  $\varepsilon_i$  are the principal strains,  $\langle x \rangle_+$  is the Macauley bracket,  $\tilde{\varepsilon}$  is the equivalent strain,  $\mathbb{K}$

is a history parameter that preserves records for previously triggered damage, which cannot decrease, and  $K_{tr0}$  is the threshold of the damage. The damage evolution law in this model is described using Eq. (21) [27].

$$g(\mathbb{K}) = \alpha_t \cdot D_t + \alpha_c \cdot D_c \quad (21)$$

where

$$D_{t,c} = 1 - \frac{K_{tr0}(1-A_{t,c})}{\mathbb{K}} - \frac{A_{t,c}}{\exp\{B_{t,c}(\mathbb{K}-K_{tr0})\}} \quad (22)$$

and  $\alpha_{t,c}$  are defined by Mazars in Ref. [27].

Two damage models have been calibrated from these LDPM results. The first one is a classical local model where the fracture energy is controlled. It is in fact the continuum damage equivalent of a crack band model. For this, the model is such that  $A_t = 1$  and the energy dissipation upon fracture can be expressed as a function of  $B_t$  and of the size of the element in which damage localizes [28]. The second model is an integral nonlocal damage model. Damage is controlled by a spatial average of the equivalent strain as described in Eq. (23) [30] where  $\tilde{\varepsilon}$  is the effective strain already described in Eq. (19), and  $\psi$  is a gaussian function with an internal length  $L_C$ .

$$\tilde{\varepsilon} = \frac{\int \psi \tilde{\varepsilon} dv}{\int \psi dv} \quad (23)$$

The average equivalent strain replaces the equivalent strain in Eq. (20). This model is fitted by adjusting two damage tensile parameters  $A_t$  and  $B_t$ , as well as the initial damage threshold parameter ( $K_{tr0}$ ). In the absence of information, the internal length, denoted as  $L_C$ , is assumed to be 3 times the maximum aggregate size, as reported in literature [29].

This model's global response is fitted by modifying the parameters to the global LDPM responses. Figure 7 shows the global responses of LDPM and damage models calculations, and table 2 shows the calculation parameters for local and non-local damage models.

**Table 2:** Damage models : model parameters

| Parameter | Non-Local Damage | Local Damage     |
|-----------|------------------|------------------|
| $E$       | 26.67 <i>GPA</i> | 26.67 <i>GPA</i> |
| $\nu$     | 0.178            | 0.178            |
| $K_{tr0}$ | $3.5e^{-5}$      | $1.7e^{-4}$      |
| $B_t$     | 5200             | 24               |
| $A_t$     | 0.85             | 1                |
| $\beta$   | 1.05             | 1.05             |

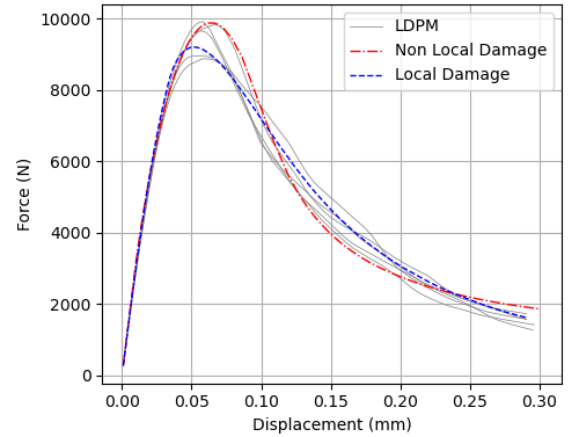


Figure 7: Load versus displacement responses for both damage models.

The damage distributions from both models are shown in figure 8. While the local model only shows damage in the central elements directly above the notch, the non-local model shows a damage zone that extends around it.

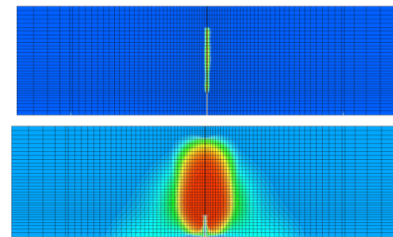


Figure 8: Damage distribution according to the local damage model (top) and nonlocal damage model (bottom). Green corresponds to values of damage equal to 0.5, red to values of damage close to 1.

The coarse-grained strains have been compared to those from both damage models. Normalised errors are calculated using Eq. (24).

Coarse-grained strains are designated by  $\varepsilon_{cg}$ , whereas strains from both damage models are denoted by  $\varepsilon_{dam}$ .

$$E_\varepsilon = \frac{\sqrt{\Delta\varepsilon : \Delta\varepsilon}}{\sqrt{\varepsilon_{dam} : \varepsilon_{dam}}} \quad (24)$$

where  $\Delta\varepsilon = \varepsilon_{cg} - \varepsilon_{dam}$ . Figure 9 shows 2D error maps comparing strains from damage models to coarse-grained LDPM calculations at time step 50 defined in figure 4. Strain errors in the non-local model are up to 80%. For the local model, the strain errors are up to 21200%. With the local model, the concentration of damage in the central parts of the local damage model causes significant errors. On the other hand, the distribution of the damage zone in the non-local damage model results in a relatively better representation of the strain for the chosen comparison region. The non-local model works better when it comes to the representation of the strain distribution, with the exception of the final two time steps where the fracture has propagated throughout the assessment region.

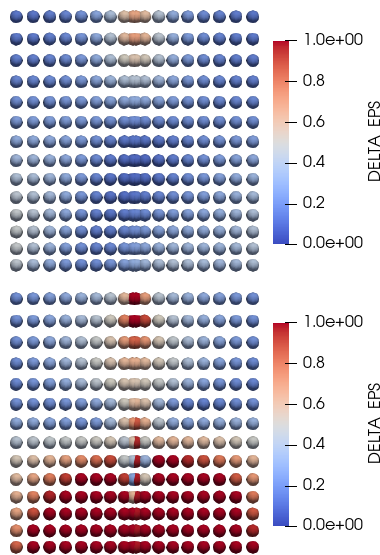


Figure 9: Normalized error map on the strains between CG-LDPM and non-local damage model (top), CG-LDPM and local damage model (bottom)

While both damage models represent rather properly the global response of the beam, significant errors still exist at the local level between the results from damage models and

those of obtained from coarse graining LDPM data. In the present section, we have assumed the value of the internal length ( $L_C$ ), using estimates that have been proposed in the literature. Finding this internal length from calibration requires classically to use size effect test data for the calibration from global responses of specimen of various sizes [31]. In the next section, local data will be used instead.

## 5 CALIBRATION FROM LOCAL RESPONSES

We shall consider now the distribution of stresses and strains obtained from LDPM results, over the window used for coarse graining in the previous section. These data are stress and strain histories upon loading the beam and during failure. The stress-strain histories in figure 10 show that close to the middle of the beam, where the macrocrack is located, responses exhibit softening. Farther from the crack location, the responses exhibit some snap-back, meaning that the horizontal stress decreases as the horizontal strain decreases, but this is not performed according to an elastic unloading. The tangent modulus is greater than upon loading. Note, however, that the state of stress is not uniaxial. There is also a vertical stress. In addition, the horizontal strain v.s. volumetric strain histories are linear. This suggests that the Poisson's ratio of the material is not changed upon irreversible local response, and it corresponds indeed to the assumption made in the isotropic damage model.

From the stress and stress distributions, the damage parameter  $D$  is calculated for each point, and at each time step, by minimizing the error between the coarse-grained and computed deformations in the three principal directions. The history parameter, denoted by  $\mathbb{K}$ , is derived from the non-local (coarse grained) strain fields according to Eqs. (19), (20), and (23). At each material point and at each load step, if the history parameter is less than the maximum value reached in the previous history, it is replaced by this maximum value. As a result, we obtain, for each coarse graining point, a map of the his-

tory parameter v.s. damage, that should follow the damage evolution law in the damage model. These maps are superimposed on the same plot, yielding figure 11.

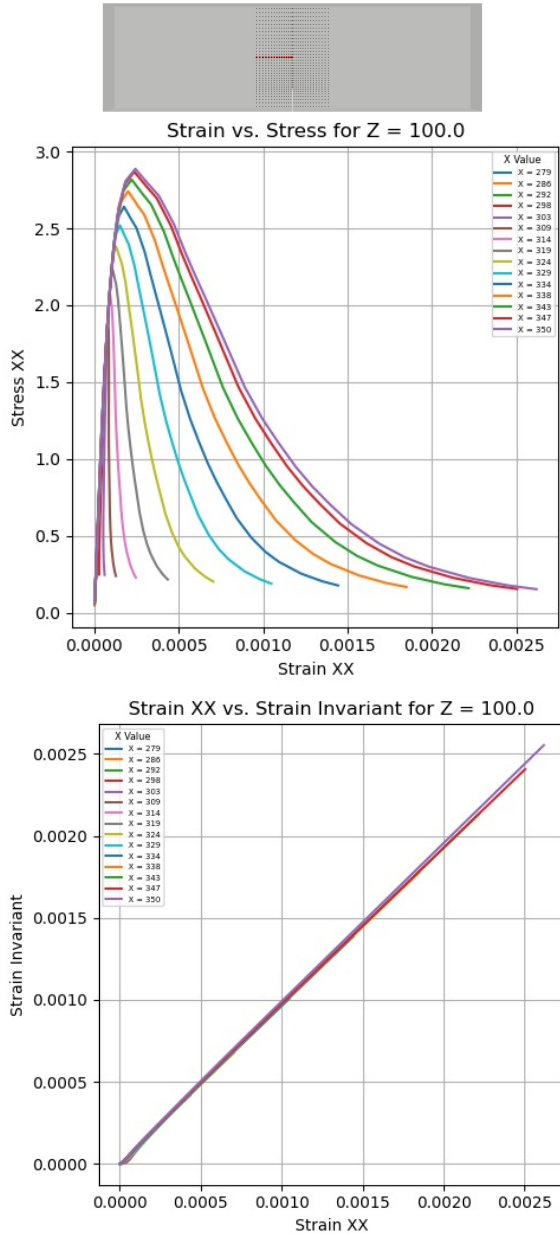


Figure 10: stress and strain histories during fracture at several points (showed on top) of the coarse graining window: horizontal stress v.s. horizontal strain histories (middle), horizontal strain versus volumetric strain (bottom).

Obviously, one needs to define the internal length  $L_C$  to perform such a calculation. Several values of the internal length, ranging from  $1D_{max}$  to  $5D_{max}$ , are considered. To avoid un-

realistic values of damage and damage threshold, the coarse graining window is not too large because very small values of damage might yield unrealistic errors. This occurs mostly when no damage has occurred and the coarse grained stress is low.

Eq. (22) is then fitted for each value of the internal length using a Levenberg-Marquardt procedure. To improve accuracy, a logarithmic scale for  $\mathbb{K}$  is used for the fit. As a result, we now have  $A_t$ ,  $B_t$ , and  $K_{tr0}$ , for every internal length  $L_C$ . We now select the best possible approximation, meaning the value of the internal length that yields the smallest possible error. Figure 11 shows the resulting fit of the damage evolution law.

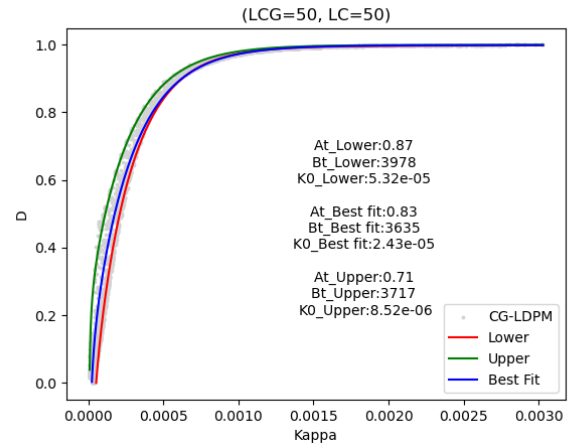


Figure 11: Damage evolution law for the best value of the internal length.

Taking the minimum of the error provides the best possible value of the internal length which turns out in this case to be equal to the coarse graining length (but this should not be automatic). We obtain then the corresponding values of the model parameters:  $A_t = 0.83$ ,  $B_t = 4212$ , and  $K_{tr0} = 4.54e^{-5}$ . All the parameters in the nonlocal damage model are now obtained from the calibration with local stress-strain histories. We observe in figure 11 that data points do not fall on a single curve. Data are noisy, but the noise results here from the error due to the postulated constitutive model compared to the LDPM response.

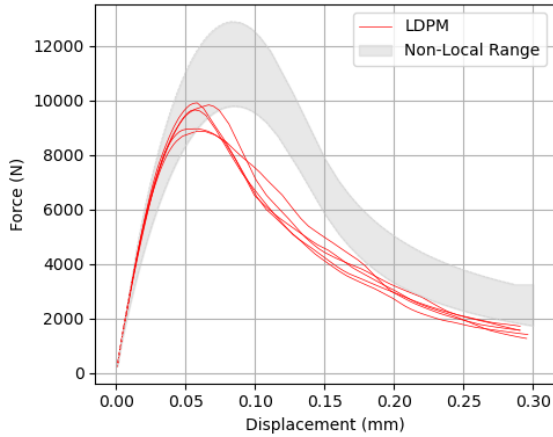


Figure 12: Prediction of the global response as a result of the local fit of the damage parameters including the internal length.

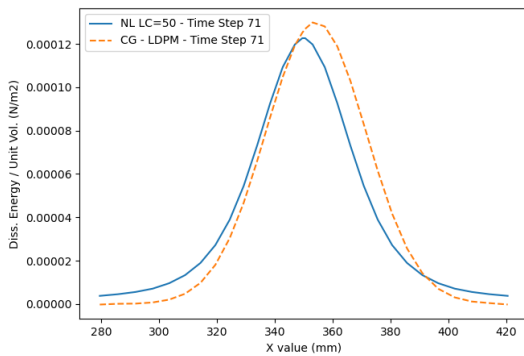


Figure 13: Profiles of energy dissipation across the FPZ at mid-height of the beam.

At this stage, it is important to check the result of this set of material parameters on the global response of the beam. Figure 12 shows the global response obtained from the nonlocal damage model. To appreciate the influence of the dispersion on the evolution law for damage, lowest and highest data points have been retained and used to fit again the equation governing the evolution of damage. We obtain an interval of values for  $A_t$ ,  $B_t$  and  $K_{tr0}$  from which two extreme responses can be computed. The LDPM responses should be located in between those extreme responses, which is almost the case. Again, this may not occur because the constitutive model is too simple. In the present case, the result can be considered satisfactory.

As a final validation of the calibration, we have also plotted the energy dissipation across the FPZ in figure. 13. The profile obtained from coarse graining directly and the profile obtained from the nonlocal model compare quite well.

## 6 CLOSURE

Lattice-based discrete approaches have been proved in the past to be much more powerful than most continuum based model when it comes to modeling fracture of concrete. Unfortunately, they are limited because they computationally too intensive. In this contribution, we have presented first a coarse graining technique that converts discrete results from LDPM to continuum based quantities such as strains and stresses. These data can serve as high-fidelity data from which a macro-scale - simplified - continuum model may be calibrated. Calibration from global responses is incomplete because the internal length entering into the regularized model cannot be obtained, unless several sizes of beams are used and the calibration repeated for each size. It is complete when considering calibration from full strains and strain fields, with the limit that the macro-scale model may be too simple and yield responses that may not be as accurate as expected. A pending issue is, however, that the predicted widths of the FPZ may not correspond to the width of the FPZ observed in the LDPM calculation. This is the subject of a companion paper presented at this conference [32].

## 7 ACKNOWLEDGMENTS

Partial financial support from the investissement d'avenir French programme (ANR-16-IDEX- 0002), the European Union's Horizon 2020 research and innovation programme EDENE under the Marie Skłodowska-Curie grant agreement No 945416, and from the Communauté d'Agglomération Pau – Béarn – Pyrénées are gratefully acknowledged. This research was performed within the E2S hub Newpores supported jointly by Université de Pau et des Pays de l'Adour and Northwestern University.

## REFERENCES

- [1] Grégoire, D., Verdon, L., Lefort, V., Grassl, P., Saliba, J., Regoin, J.P., Loukili, A., Pijaudier-Cabot, G., Mesoscale analysis of failure in quasi-brittle materials: comparison between lattice model and acoustic emission data, *Int. Num. Anal. Meth. Geomechanics*, 39, 1639-1664 (2015).
- [2] Haidar, K. Pijaudier-Cabot, G., Dube, J.F., Loukili, A., Correlation between internal length, fracture process zone and size effect in mortar and model materials, *Materials and Structures*, 38, 201-210 (2005).
- [3] Hillerborg, A., Modeer, M., Petersson, P.E., Analysis of crack formation and crack growth in concrete by means of fracture mechanics and finite elements, *Cement Concrete Res.*, 6, 773-782 (1976).
- [4] Mazars, J., Pijaudier-Cabot, G., Continuum damage theory: application to concrete, *J. Engrg. Mech. ASCE*, 115, 345-365 (1989).
- [5] Desmorat, R., Gatuingt, F., Ragueneau, F. Nonlocal anisotropic damage model and related computational aspects for quasi-brittle materials, *Engrg. Fract. Mech.*, 74, 1539-1560 (2007).
- [6] Fichant, S., La Borderie, C., Pijaudier-Cabot, G., Isotropic and anisotropic descriptions of damage in concrete structures, *Int. J. Mechanics of Cohesive Frictional Materials*, 4, 339-359 (1999).
- [7] Grassl, P., Jirasek, M., Damage-plastic model for concrete failure, *Int. J. Solids Struct.*, 43, 7166-7196 (2006).
- [8] Caner, F.C., Bažant, Z.P. Microplane model M7 for plain concrete: I. Formulation, *Journal of Engineering Mechanics ASCE*, 139, 1714-1723 (2013).
- [9] Bažant, Z.P., Nguyen, H., Donmez, A.A., Critical comparison of phase-field, peridynamics, and crack band model m7 in light of gap test and classical fracture tests, *J. Applied Mechanics, ASME*, 89, 061008 (2022).
- [10] Cundall, P.A., A computer model for simulating progressive, large-scale movements in block rock systems, *Proc. Symposium Int. Soc. Rock Mech. France*, 129-136 (1971).
- [11] Zubelewicz, A., Bažant, Z.P., Interface modeling of fracture in aggregate composites, *Journal of Engineering Mech. ASCE*, 113, 1619-1630 (1987).
- [12] Bažant, Z.P., Tabbara, M.R., Kazemi, M.T., Pijaudier-Cabot, G., Random particle model for fracture of aggregates or fiber composites, *J. Engrg. Mech. ASCE*, 116, 1686-1705 (1990).
- [13] Bolander, J.E., Elias, J., Cusatis, G., Nagai, K., Discrete mechanical models for concrete fracture, *Engrg. Fract. Mechanics*, 257, 108030 (2021).
- [14] Ashari, S. E., Buscarnera, G., Cusatis, G., A lattice discrete particle model for pressure-dependent inelasticity in granular rocks. *International Journal of Rock Mechanics and Mining Sciences*, 91:49-58 (2017).
- [15] Pijaudier-Cabot, G., Khoury, J., *Damage Mechanics for Quasi-Brittle Materials: Continuum and Lattice Descriptions*. In: Silberschmidt, Vadim (eds.) *Comprehensive Mechanics of Materials*, 1:303?324. Oxford, Elsevier (2024).
- [16] Grassl, P., Grégoire, D., Solano, L. R., Pijaudier-Cabot, G. (2012). Meso-scale modelling of the size effect on the fracture process zone of concrete. *International Journal of Solids and Structures*, 49:1818-1827.

- [17] Kirchdoerfer, T., Ortiz, M. Data Driven Computational Mechanics. *Comput Meths Appl Mech Eng* 304, 81-101 (2016).
- [18] Cusatis, G., Pelessone, D., Mencarelli, A., Lattice discrete particle model (ldpm) for failure behavior of concrete. i: Theory. *Cement and Concrete Composites*, 33:881-890 (2011).
- [19] Han, L., Pathirage, M., Akono, A.-T., Cusatis, G., Lattice discrete particle modeling of size effect in slab scratch tests. *Journal of Applied Mechanics*, 88:021009 (2021).
- [20] Schaufert, E. A., Cusatis, G., Lattice discrete particle model for fiber-reinforced concrete. I: Theory. *J. Engrg. Mech. ASCE*, 138:826-833, (2012).
- [21] Feng, J., Sun, W., Chen, L., Chen, B., Arkin, E., Du, L., Pathirage, M., Engineered Cementitious Composites using Chinese local ingredients: Material preparation and numerical investigation. *Case Studies in Construction Materials*, 16:e00852 (2022).
- [22] Zhu, Z., Pathirage, M., Wang, W., Troemner, M., Cusatis, G., Lattice discrete particle modeling of concrete under cyclic tension-compression with multi-axial confinement. *Construction and Building Materials*, 352:128985 (2017).
- [23] Glasser, B.J., Goldhirsch, I., Scale dependence, correlations, and fluctuations of stresses in rapid granular flows, *Phys. Fluids* 13, 407-420 (2001).
- [24] Goldhirsch, I., Goldenberg, C., On the microscopic foundations of elasticity, *Eur. Phys. J. E*, 9, 245-251 (2002).
- [25] Pathirage, M., Tong, D., Thierry, F., Cusatis, G., Grégoire, D., Pijaudier-Cabot, G., Discrete modeling of concrete failure and size-effect. *Theoretical and Applied Fracture Mechanics*, 124:103738 (2023).
- [26] Grégoire, D., Rojas-Solano, L., Pijaudier-Cabot, G., Failure and size effect for notched and unnotched concrete beams, *Int. J. Num. and Anal. Meths. Geomechanics*, 37, 1434-1452 (2013).
- [27] Mazars, J., A description of micro-and macro-scale damage of concrete structures. *Engineering fracture mechanics*, 25:729-737 (1986).
- [28] La Borderie, C. (2003). *Stratégies et modeles de calculs pour les structures en béton. Habilitation a diriger des recherches*, Université de Pau et des Pays de l'Adour, France.
- [29] Bažant, Z.P., Pijaudier-Cabot, G., Measurement of the characteristic length of nonlocal continuum, *J. Engrg. Mech. ASCE*, 115, 755-767 (1989).
- [30] Pijaudier-Cabot, G., and Bažant, Z.P., Nonlocal damage theory. *J. Engineering. Mech. ASCE*, 113, 1512-1533 (1987).
- [31] Le Bellego, C., Dube, J.F., Pijaudier-Cabot, G., Gérard, B., Calibration of non-local damage model from size effect tests, *Eur. J. Mech. A/Solids*, 22, 33-46 (2003).
- [32] Khoury, J., Pijaudier-Cabot, G., Cusatis, G., Calibrating a Damage Model from Lattice Results, *Proc. FaMCoS 12*, B.A. Pichler et al. (eds), (2025).